Supporting Information

Elucidating the exceptional halide ion etching of bimetallic Ag-Cu oxides for efficient adsorption and porous nanostructural formation

Meng Zhang,[a] Fuzhu Liu, [b] Hongliang Yang,[c] Zhanglian Xu,*[a] Junjie Wang,[c] Yutong Gong*[c]

[a]*School of Nuclear Science and Technology, Xi'an Jiaotong University, Xi'an, Shaanxi 710049, P. R. China.*
[b]*School of Materials Science and Engineering, Xi'an Jiaotong University, Xi'an, Shaanxi 710049, P. R. China.*
[c]*State Key Laboratory of Solidification Processing, School of Materials Science and Engineering, Northwestern Polytechnical University, Xi'an, Shaanxi, 710072, P. R. China*

Corresponding authors. E-mail: xuzhanglian@xjtu.edu.cn (Z. X.); gongyutong@nwpu.edu.cn (Y. G.).

Adsorption data fitting：

(1) Langmuir and Freundlich models were used to fit the adsorption isotherm data according to the following equations, respectively.

$$\frac{C_e}{q_e} = \frac{1}{q_m K_L} + \frac{1}{q_m} C_e \qquad (1)$$

$$\ln q_e = \ln K_F + \frac{1}{n} \ln C_e \qquad (2)$$

where q_e (mg/g) represented the uptake capacity at equilibrium, C_e (mg/L) was the equilibrium concentration of solution, q_m (mg/g) was the theoretical maximum uptake capacity of the adsorbent. K_L was the Langmuir constant; n and K_F were the Freundlich constants.

(2) The pseudo-first- and second-order models were used to fit the kinetic data to investigate the adsorption mechanism. and the corresponding formula can be seen below.

$$\lg(q_e - q_t) = \lg q_e - \frac{k_1}{2.303} t \qquad (3)$$

$$\frac{t}{q_t} = \frac{1}{k_2 q_e^2} + \frac{t}{q_e} \qquad (4)$$

where q_t and q_e (mmol/g) represented the adsorption capacity at t (min) and equilibrium time, respectively; k_1 (min^{-1}) and k_2 (g mg^{-1} min^{-1}) were rate constants of the pseudo-first-order and pseudo-second-order model respectively.
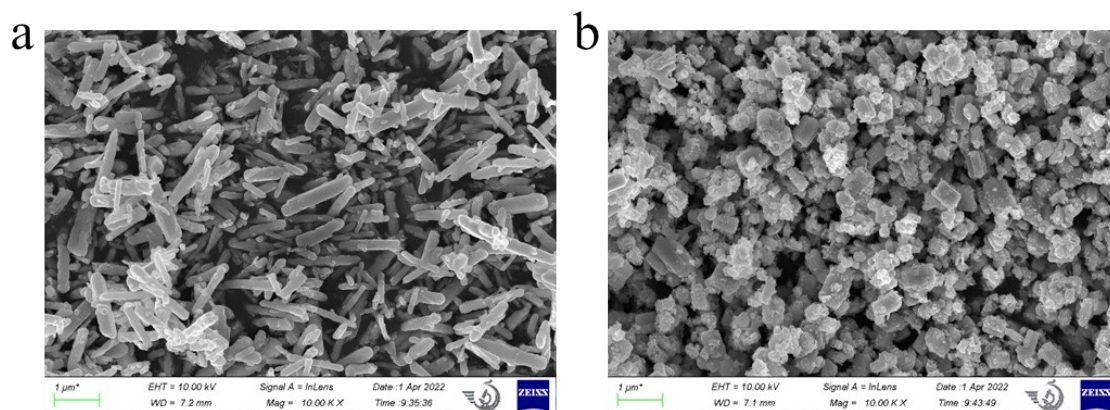
Figures

Figure S1. SEM images of (a) $Ag_2Cu_2O_3$ and (b) $Ag_2Cu_2O_4$.
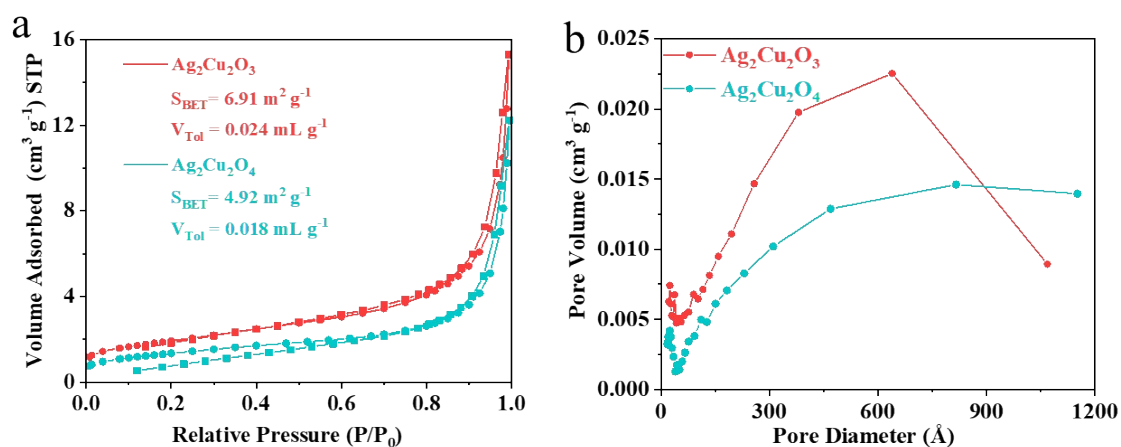
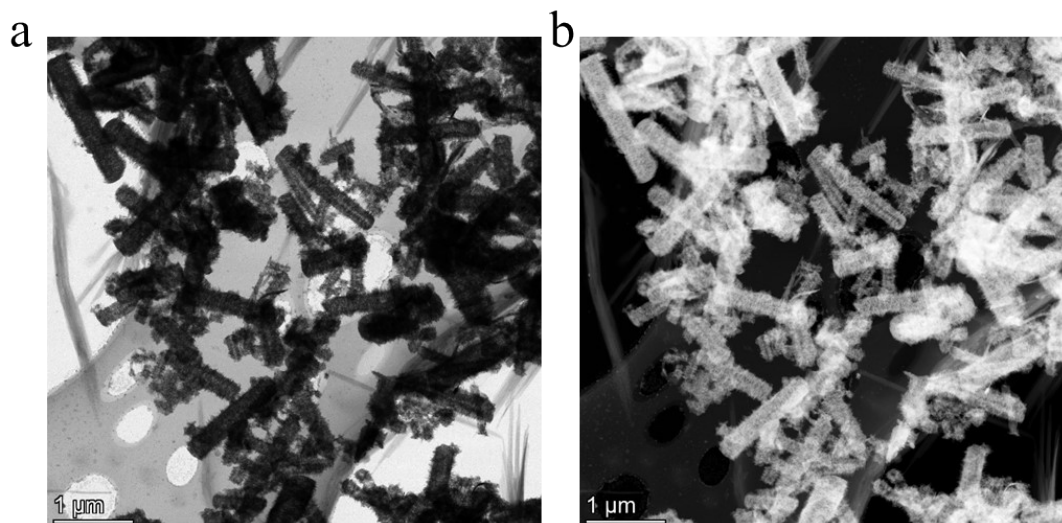**Figure S2.** (a) N_2 sorption isotherms and (b) pore size distributions of $Ag_2Cu_2O_3$ and $Ag_2Cu_2O_4$ samples.

Figure S3. (a) TEM and (b) HAADF-STEM images of $Ag_2Cu_2O_3$ etched by I^- for 24 h (the initial concentration of I^- was 7 mM).
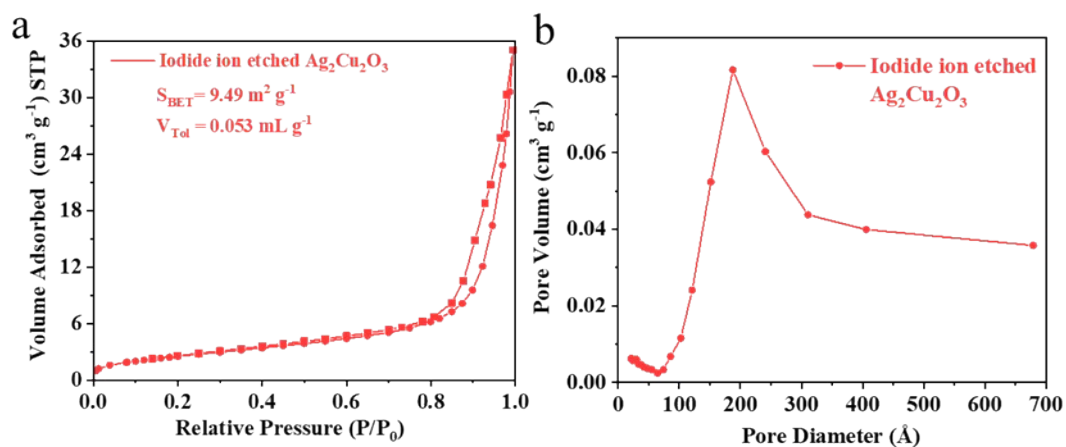
3

Figure S4. (a) N_2 sorption isotherms and (b) pore size distribution of $Ag_2Cu_2O_3$ samples after I^- etching (the initial concentration of I^- was 7 mM).
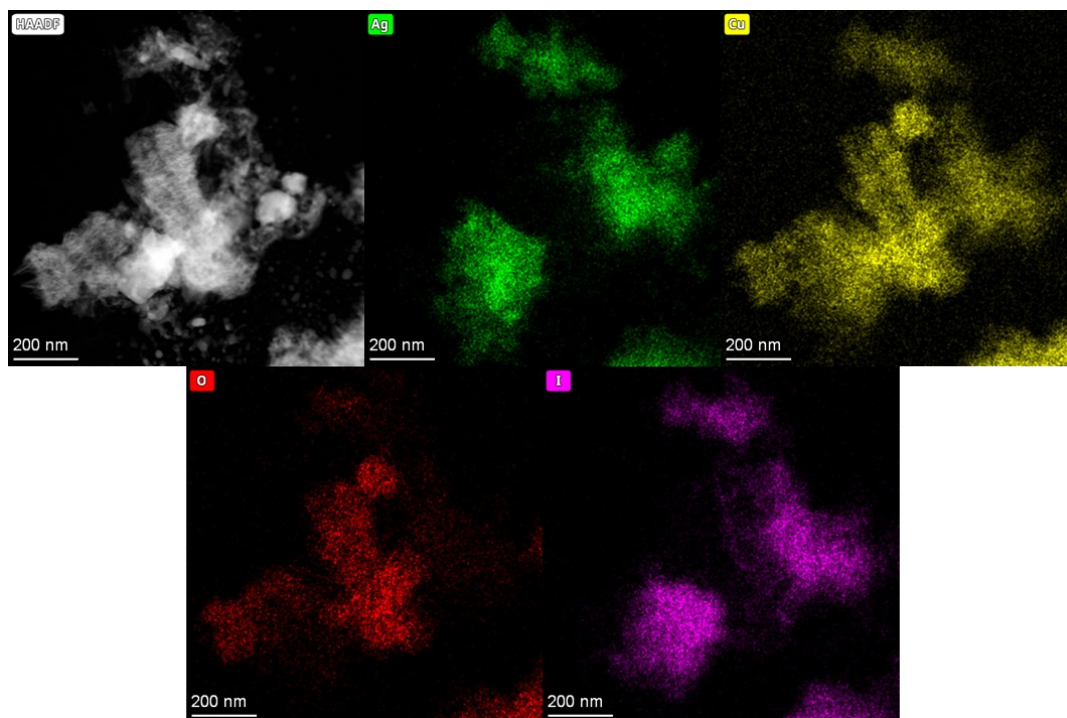

Figure S5. HAADF-STEM and corresponding elemental mapping images of $Ag_2Cu_2O_3$ etched by I^- for 24 h (the initial concentration of I^- was 7 mM).
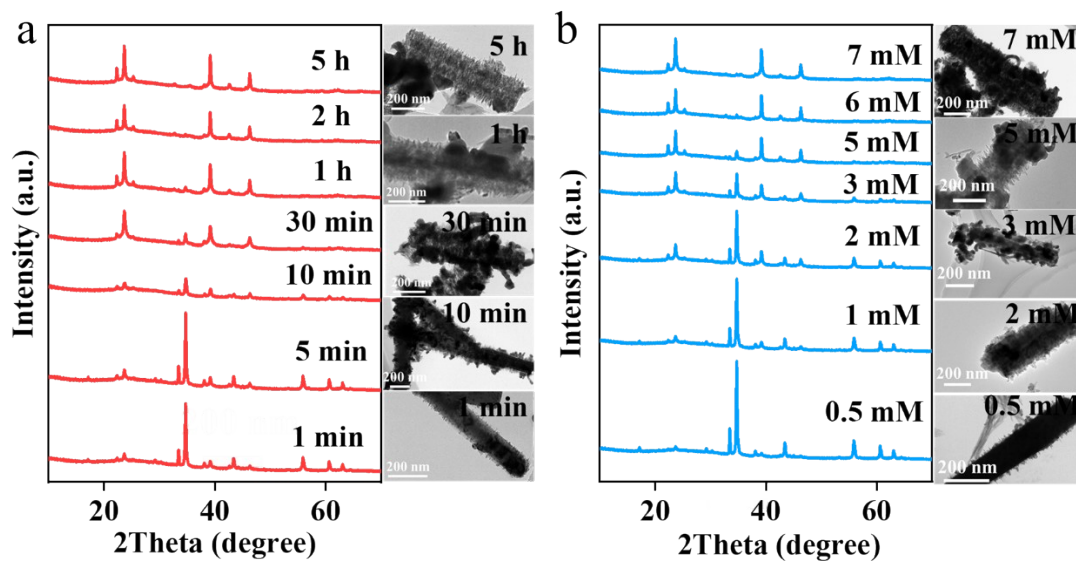
Figure S6. XRD patterns and the corresponding TEM images of $Ag_2Cu_2O_3$ etched by I^- as a function of (a) etching time (the initial concentration of I^- was 7 mM) and (b) initial I^- concentration.

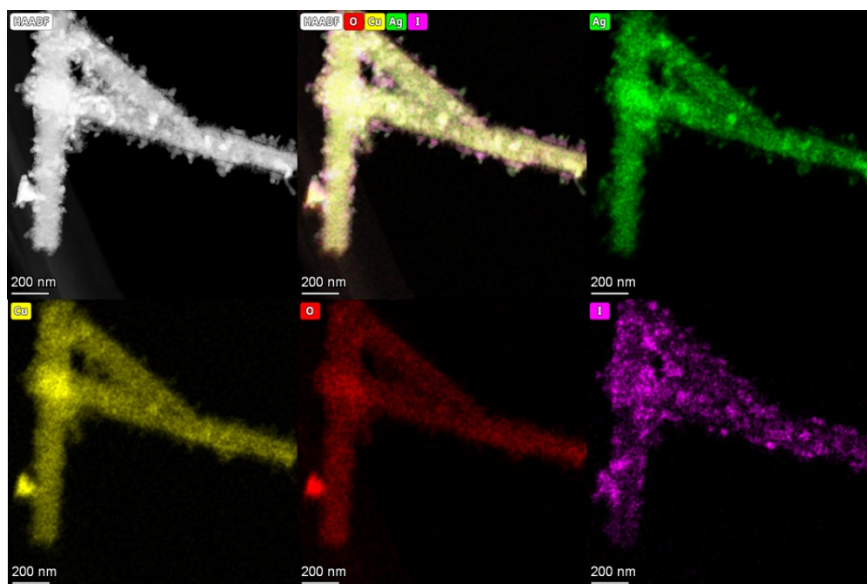**Figure S7.** HAADF-STEM and corresponding elemental mapping images of $Ag_2Cu_2O_3$ etched by I^- (the initial concentration of I^- was 7 mM)) for 10 min.
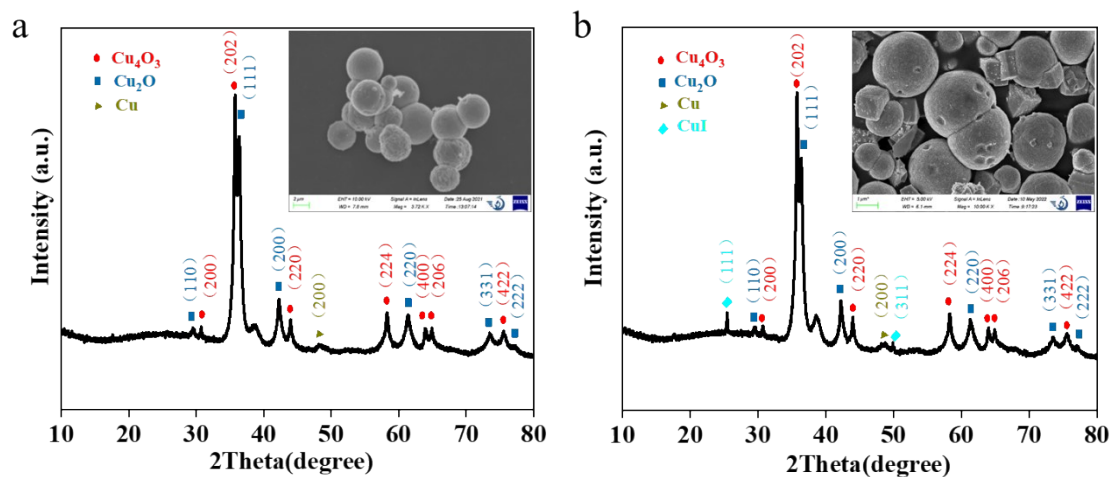
Figure S8. XRD patterns and SEM images (inset) of the synthesized Cu_4O_3 (a) before and (b) after interaction with iodide ions.

Notes: The characteristic peaks and morphology of the Cu_4O_3 phase were almost unchanged after contacting with iodide ions, and no CuO phase was observed, suggesting that Cu_4O_3 did not undergo iodide etching. The appearance of the CuI phase in Figure S8b may be attributed to the reaction of other phases in the sample such as Cu_2O or Cu phase with iodide ions.
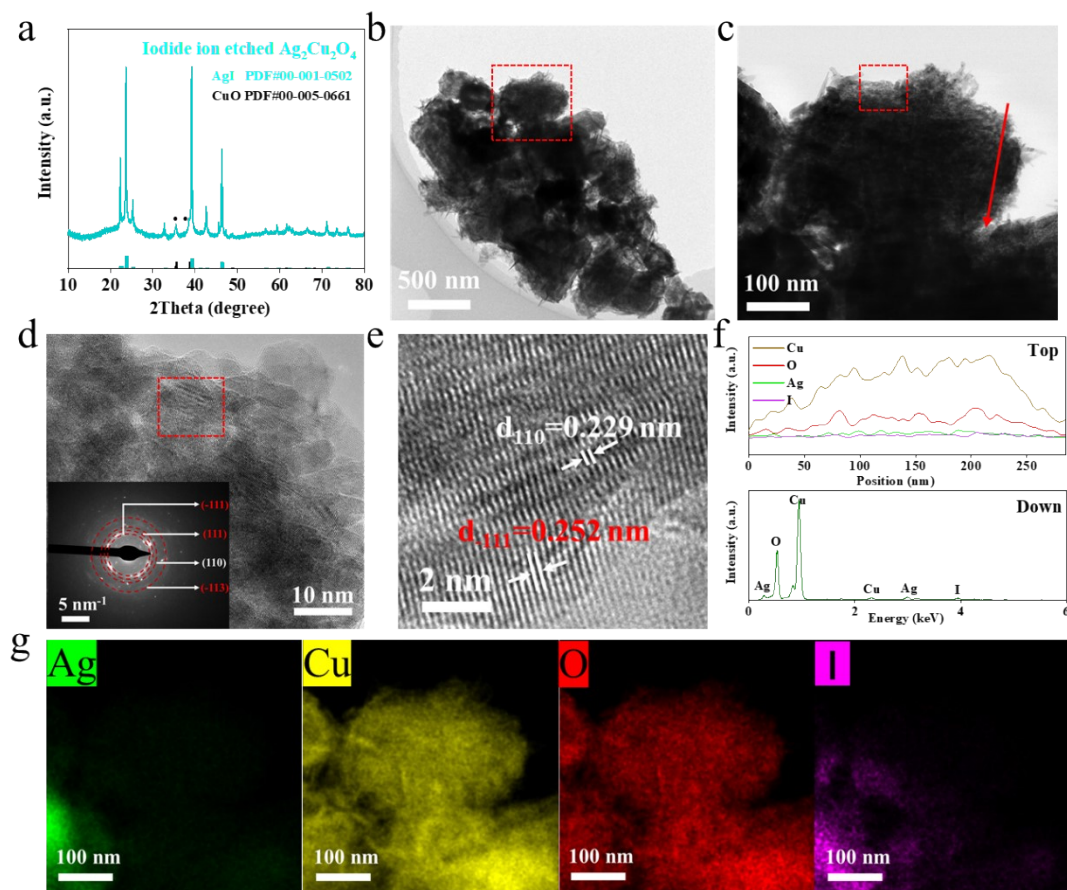
Figure S9. (a) PXRD pattern and (b-e) TEM images of $Ag_2Cu_2O_4$ etched by iodide ions. The inset of Figure S8d is the selected area electron fraction (SAED) spectrum. (f) Representative STEM-EDX line profiles and (g) elemental mapping images of elements of $Ag_2Cu_2O_4$ etched by iodide ions.
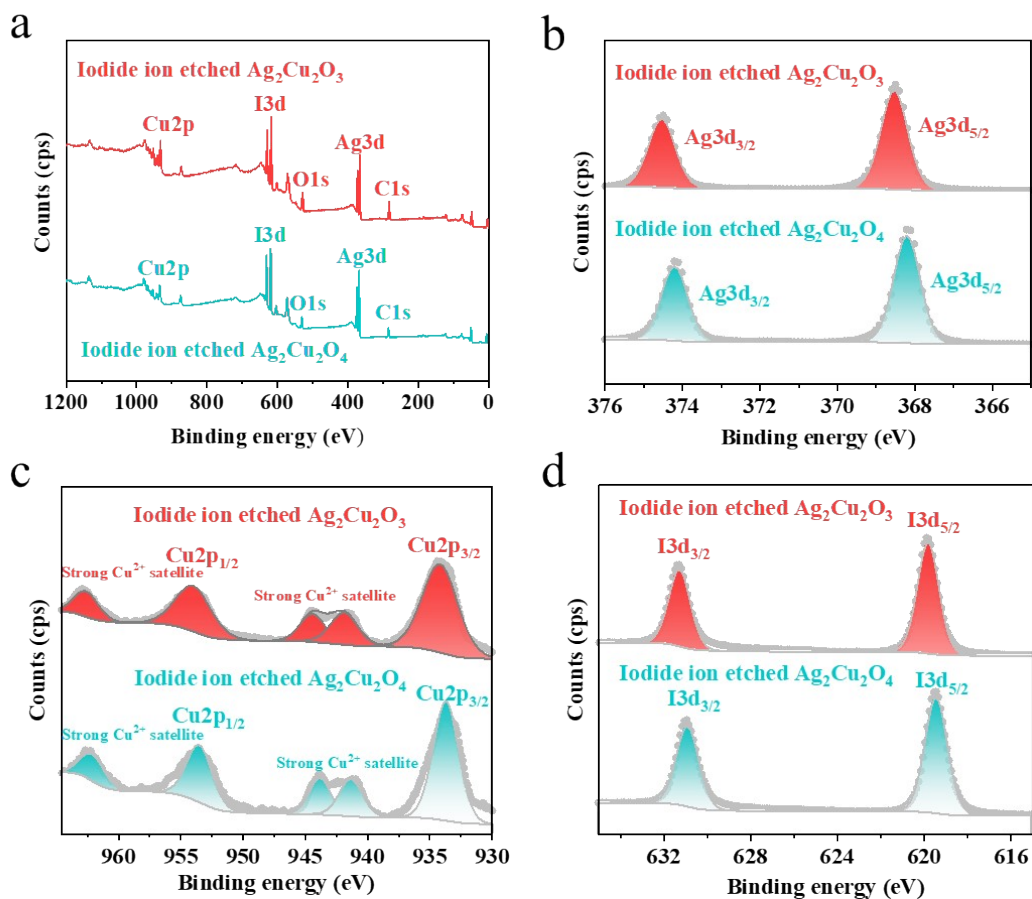
Figure S10. XPS spectra of $Ag_2Cu_2O_3$ and $Ag_2Cu_2O_4$ before and after uptake of I^-. (a) Survey scan; (b) Ag 3d and (c) Cu 2p spectra before and after I^- uptake; (d) I 3d spectra after I^- uptake.
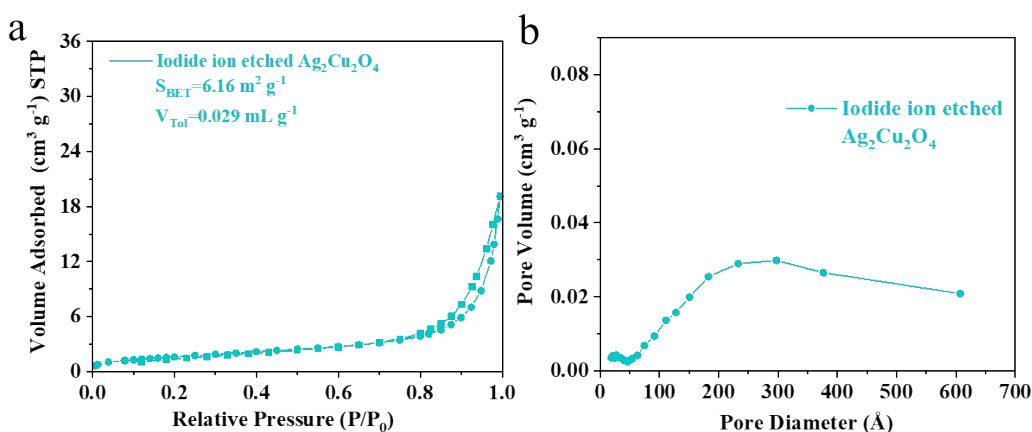
Figure S11. (a) N_2 sorption isotherms and (b) pore size distribution of $Ag_2Cu_2O_4$ samples after I^- etching (the initial concentration of I^- was 7 mM).
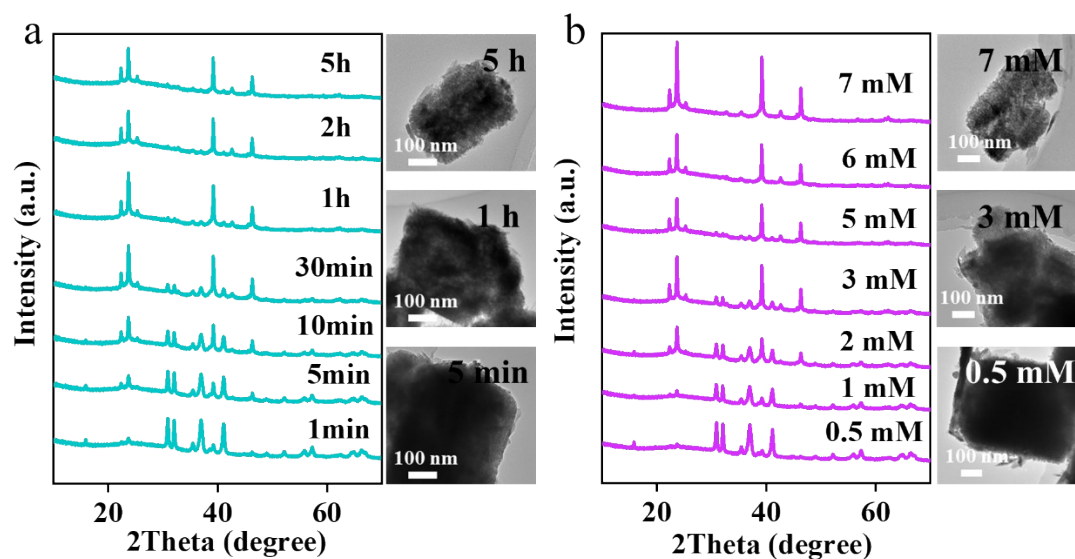
Figure S12. XRD patterns and the corresponding TEM images of $Ag_2Cu_2O_4$ etched by I^- as a function of (a) etching time (the initial concentration of I^- was 7 mM) and (b) initial I^- concentration.
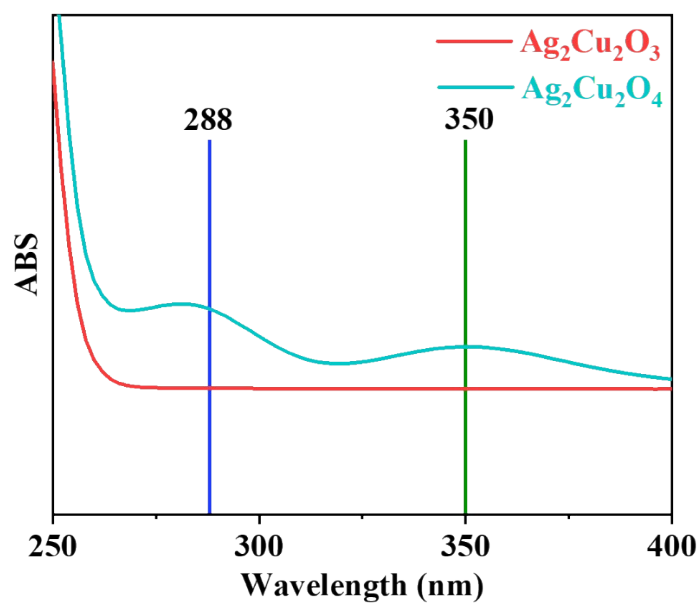
Figure S13. UV-Vis absorption spectra of the supernatants obtained after I^- etching of bimetallic Ag-Cu oxides for 10 min (the initial concentration of I^- was 7 mM).
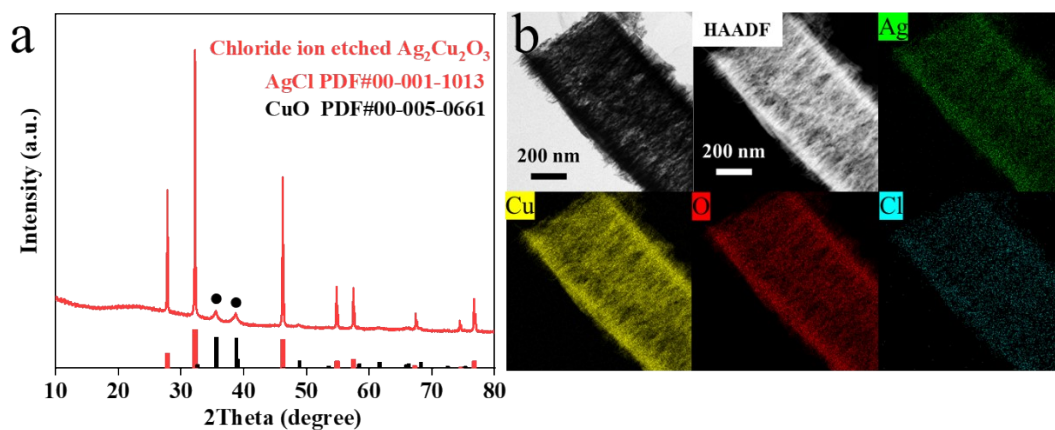
Figure S14. (a) PXRD pattern and (b) TEM images and elemental mapping images of the Cl⁻ etched $Ag_2Cu_2O_3$ samples (the initial concentration of Cl⁻ was 7 mM).
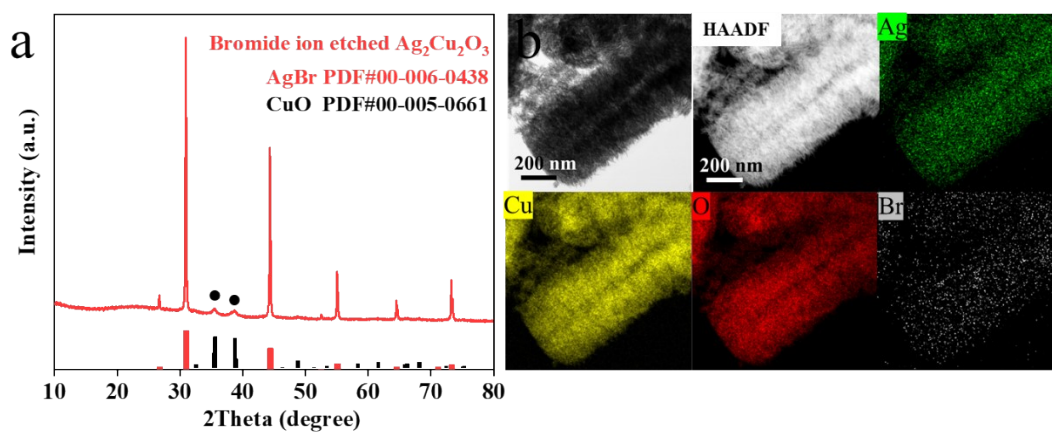
Figure S15. (a) PXRD pattern and (b) TEM images and elemental mapping images of the Br⁻ etched $Ag_2Cu_2O_3$ samples (the initial concentration of Br⁻ was 7 mM).
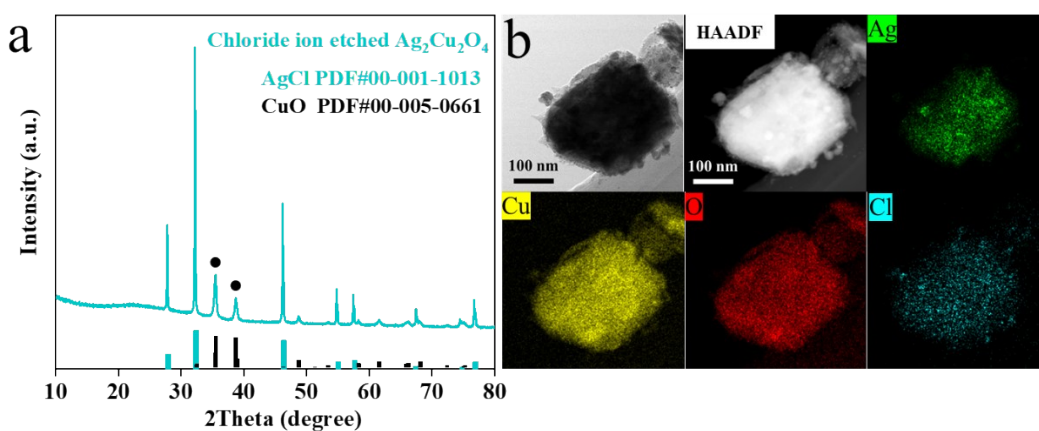
Figure S16. (a) PXRD pattern and (b) TEM images and elemental mapping images of the Cl⁻ etched $Ag_2Cu_2O_4$ samples (the initial concentration of Cl⁻ was 7 mM).
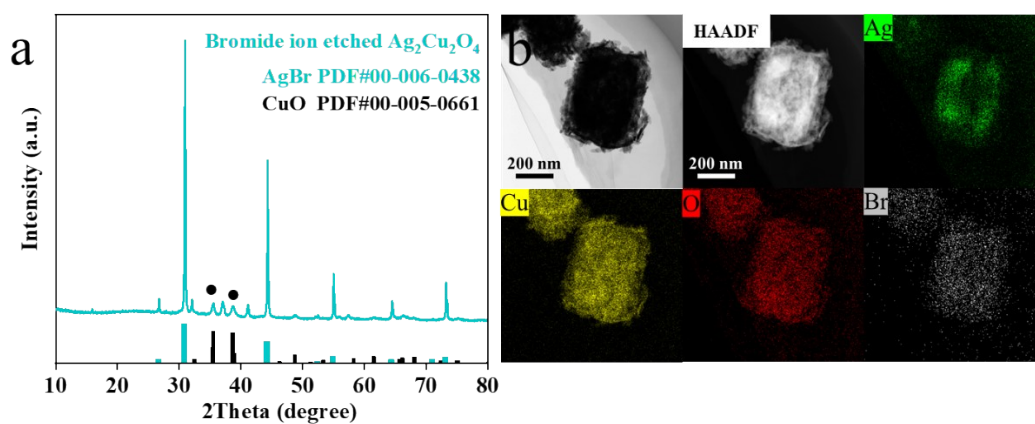
Figure S17. (a) PXRD pattern and (b) TEM images and elemental mapping images of the Br⁻ etched $Ag_2Cu_2O_4$ samples (the initial concentration of Br⁻ was 7 mM).
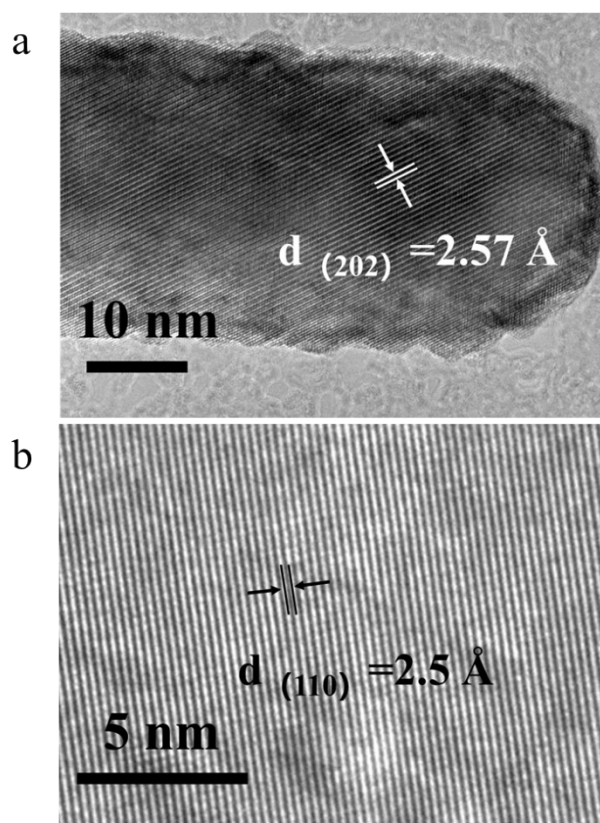
Figure S18. HRTEM images of (a) $Ag_2Cu_2O_3$ and (b) $Ag_2Cu_2O_4$.

11

Ag   Cu   O   I   Br   Cl

a

$Ag_2Cu_2O_3$(Ag-top-2)

E_{ad}= -2.99 eV

$Ag_2Cu_2O_3$(Ag-bridge-1)

E_{ad}= 5.01 eV

$Ag_2Cu_2O_3$(Ag-bridge-2)

E_{ad}= -3.10 eV

$Ag_2Cu_2O_3$(Ag-hollow-1)

E_{ad}= -3.10 eV

$Ag_2Cu_2O_3$(Ag-hollow-2)

E_{ad}= -2.99 eV

$Ag_2Cu_2O_3$(Cu-top)

E_{ad} = -2.98 eV

b

$Ag_2Cu_2O_3$(Ag-top-1)

E_{ad}= -4.09 eV

$Ag_2Cu_2O_3$(Ag-top-2)

E_{ad}= -3.17 eV

$Ag_2Cu_2O_3$(Ag-bridge-2)

E_{ad}= -3.28 eV

$Ag_2Cu_2O_3$(Ag-hollow-1)

E_{ad}= -3.27 eV

$Ag_2Cu_2O_3$(Ag-hollow-2)

E_{ad}= -3.17 eV

$Ag_2Cu_2O_3$(Cu-top)

E_{ad} = -3.16 eV

c

$Ag_2Cu_2O_3$(Ag-top-1)

E_{ad}= -4.17 eV

$Ag_2Cu_2O_3$(Ag-top-2)

E_{ad}= -3.45 eV

$Ag_2Cu_2O_3$(Ag-bridge-2)

E_{ad}= -3.57 eV

$Ag_2Cu_2O_3$(Ag-hollow-1)

E_{ad}= -3.57 eV

$Ag_2Cu_2O_3$(Ag-hollow-2)

E_{ad}= -3.45 eV

$Ag_2Cu_2O_3$(Cu-top)

E_{ad} = -4.49 eV

Figure S19. Adsorption configurations of I (a), Br (b), and Cl (c) on 202 surfaces of $Ag_2Cu_2O_3$.
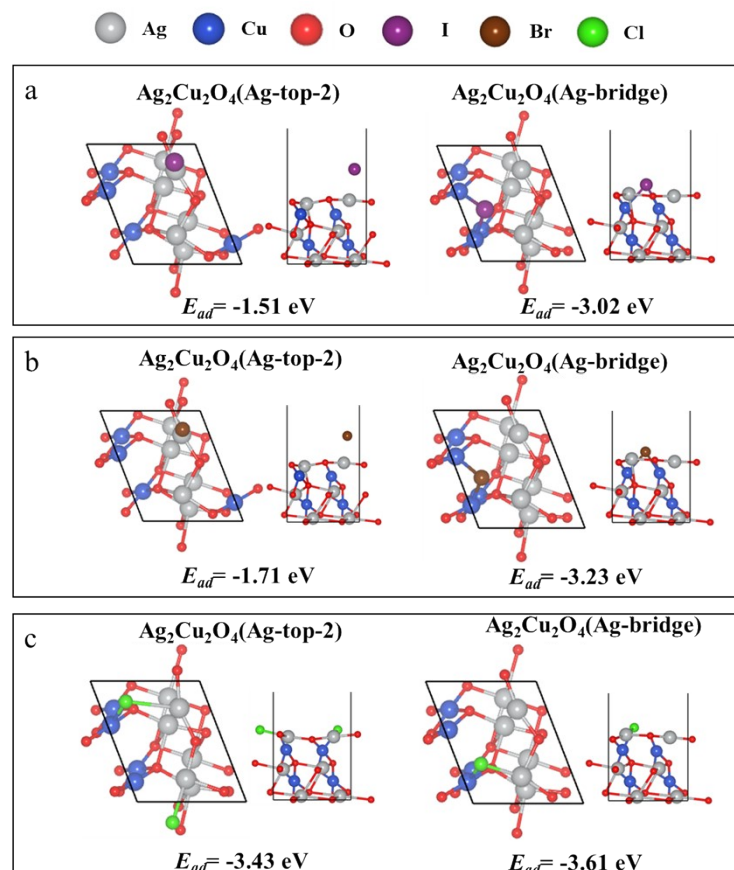
Figure S20. T Adsorption configurations of I (a), Br (b), and Cl (c) on 110 surfaces of $Ag_2Cu_2O_4$.
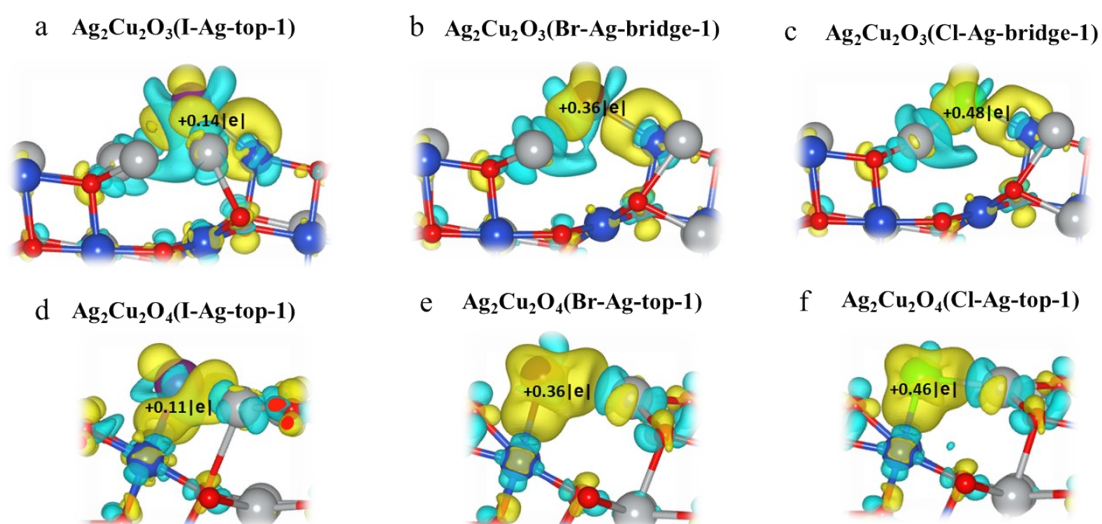
Figure S21. Differential charge density diagrams of $Ag_2Cu_2O_3$ and $Ag_2Cu_2O_4$ after adsorption of I (a, d), Br (b, e), and Cl (c, f).
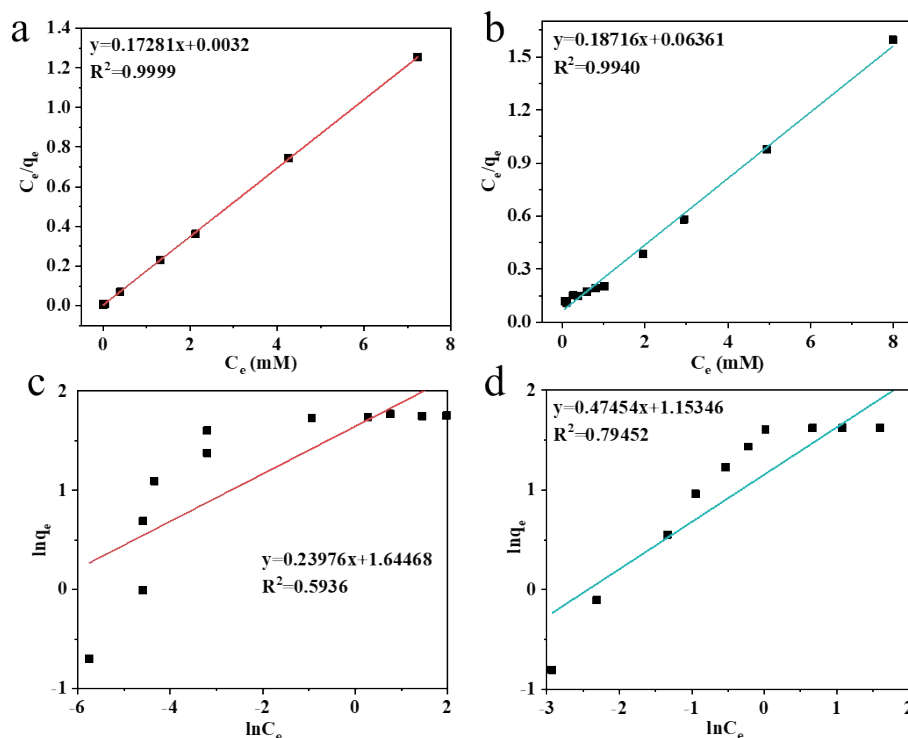
Figure S22. Langmuir models of (a) $Ag_2Cu_2O_3$ and (b) $Ag_2Cu_2O_4$ and Freundlich models of (c) $Ag_2Cu_2O_3$ and (d) $Ag_2Cu_2O_4$ for I⁻ adsorption.
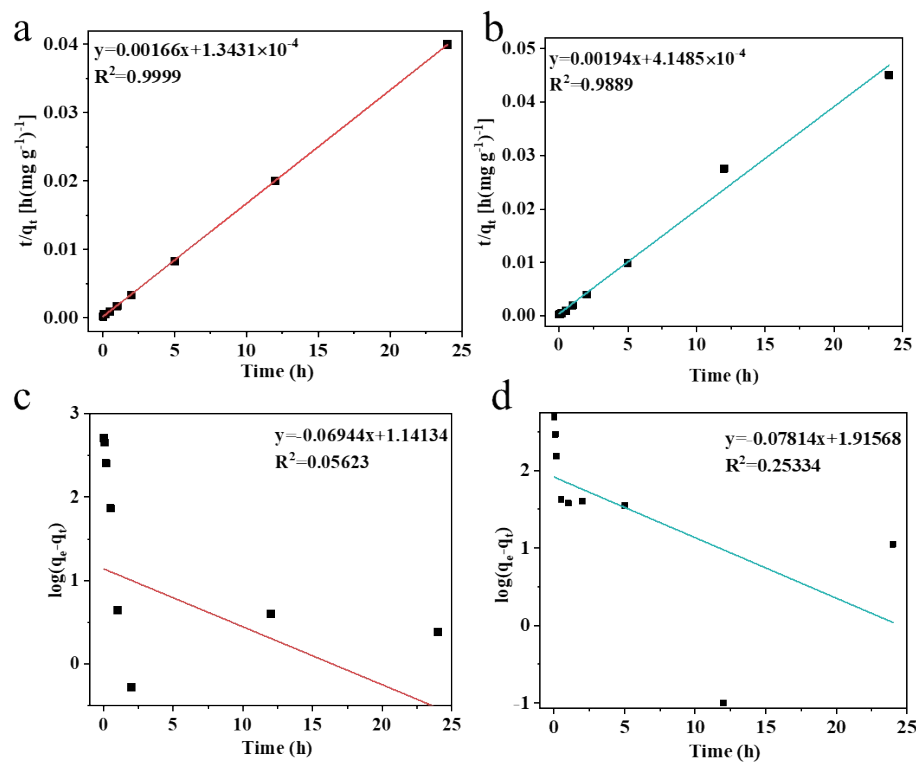
Figure S23. Pseudo-second-order kinetics models of (a) $Ag_2Cu_2O_3$ and (b) $Ag_2Cu_2O_4$ and pseudo-first-order kinetics models of (c) $Ag_2Cu_2O_3$ and (d) $Ag_2Cu_2O_4$ for I⁻ adsorption.
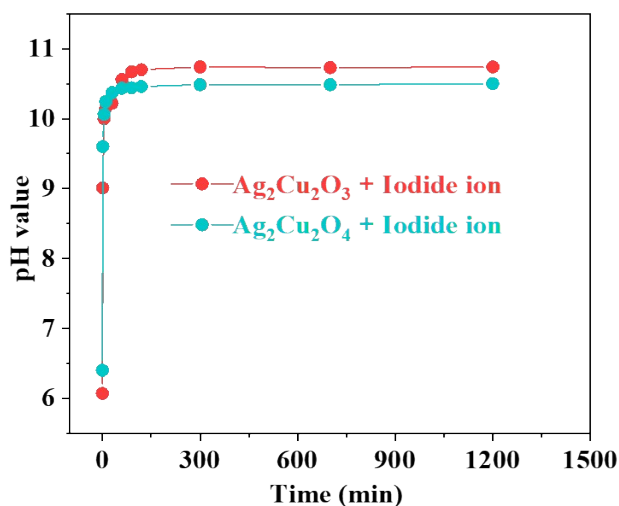
Figure S24. The pH change of I⁻ solution depending on the contacting time with bimetallic Ag-Cu oxides (the initial concentration of I⁻ was 7 mM).
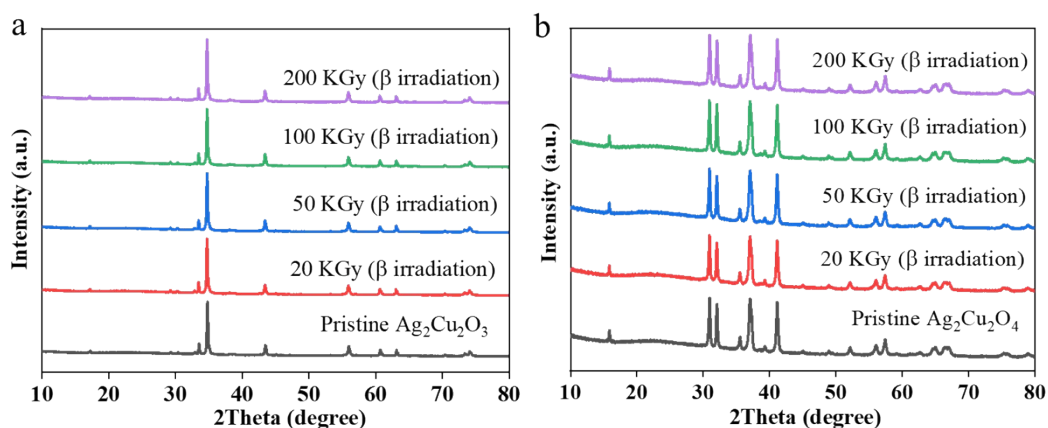
Figure S25. PXRD patterns of pristine $Ag_2Cu_2O_3$ (a) and $Ag_2Cu_2O_4$ (b) and their corresponding samples after β irradiation.
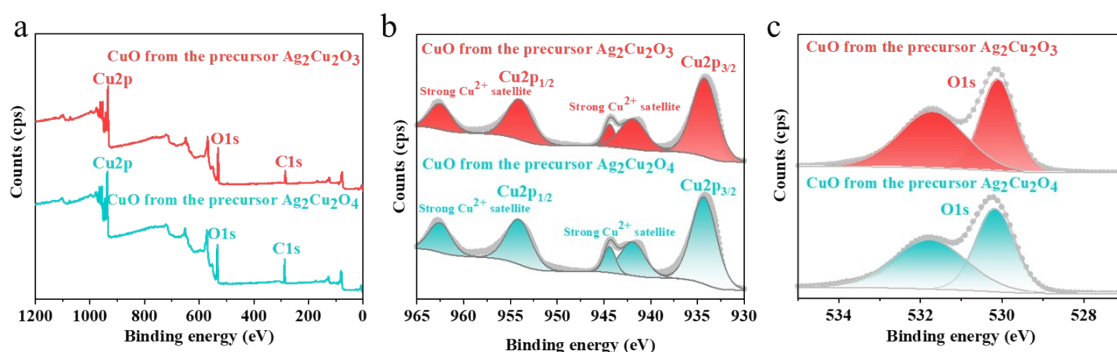
Figure S26. XPS spectra of porous CuO nanostructures after dissolving AgI crystals from the I⁻ etched $Ag_2Cu_2O_3$ and $Ag_2Cu_2O_4$ (the initial concentration of I⁻ was 7 mM)⁻. (a) Survey scan; High-resolution (b) Cu 2p and (c) O 1s spectra.
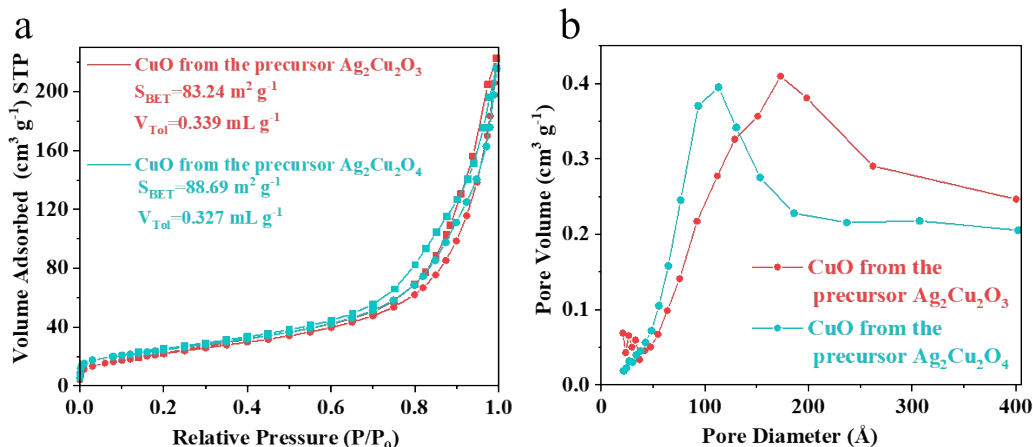
Figure S27. (a) N_2 sorption isotherms and (b) pore size distribution of porous CuO nanostructures after dissolving AgI crystals from the I⁻ etched $Ag_2Cu_2O_3$ and $Ag_2Cu_2O_4$.
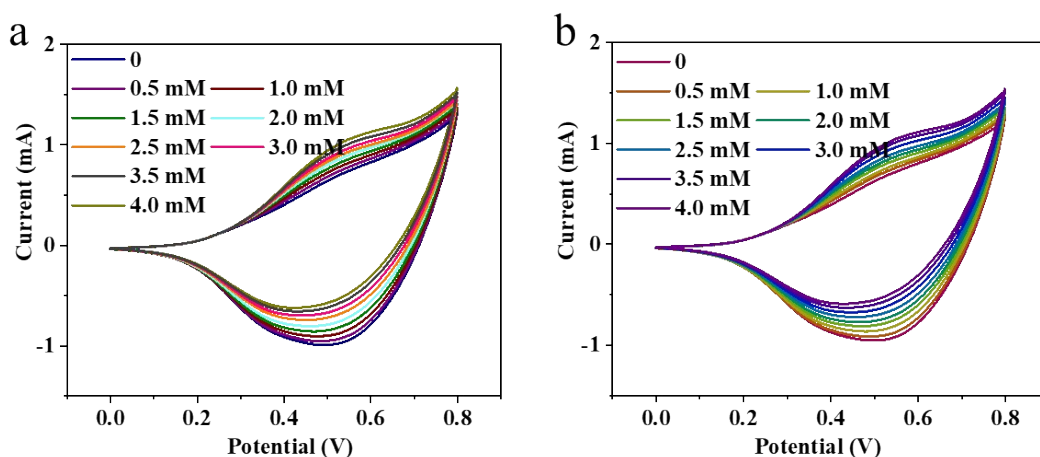
Figure S28. Cyclic voltammograms (CVs) of porous CuO electrodes obtained from (a) $Ag_2Cu_2O_3$ and (b) $Ag_2Cu_2O_4$ in 0.1 M NaOH containing 0-4.0 mM glucose at a scan rate of 100 mV s⁻¹.
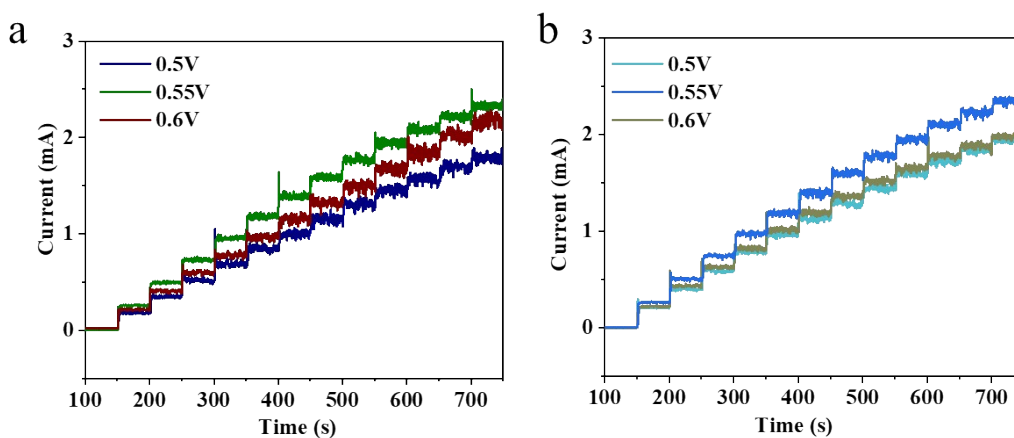
Figure S29. Amperometric i-t response of porous CuO electrodes obtained from (a) $Ag_2Cu_2O_3$ and (b) $Ag_2Cu_2O_4$ after the addition of 0.5 mM glucose at different applied potentials (vs. Ag/AgCl).
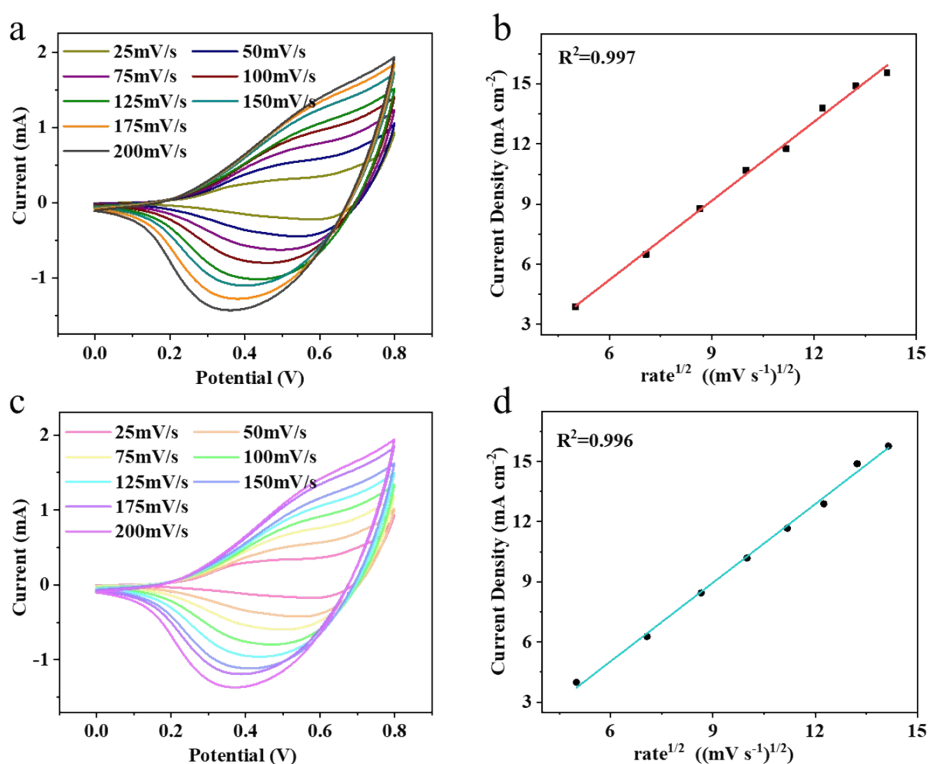
Figure S30. CVs of porous CuO nanomaterial electrodes obtained from the precursors of (a) $Ag_2Cu_2O_3$ and (c) $Ag_2Cu_2O_4$ in 0.1 M NaOH with 2.0 mM glucose at different scan rates. (b, d) Plots of the anodic peak current density versus the square root of the scan rate ($v^{1/2}$) derived from (a, c).

Notes: To investigate the effect of the potential scan rate, the CV curves of both porous CuO electrodes were performed toward 2.0 mM glucose at different scan rates from 25 to 200 mV s^{-1}, as shown in Fig. S23, and their corresponding plots of the peak current (I_{pa}) versus the square root of scan rate presented a good linear relationship with the regression equation of I_{pa} (μA) = 1.313 $v^{1/2}$ ($(mV\ s^{-1})^{1/2}$) + 2.648 (R^2 = 0.997) for porous CuO rods and I_{pa} (μA) = 1.309 $v^{1/2}$ ($(mV\ s^{-1})^{1/2}$) + 2.820 (R^2 = 0.996) for porous CuO cubes, showing the diffusion-controlled process of glucose electrooxidation reaction on both porous CuO electrodes.

Tables

Table S1. Comparison of I⁻ adsorbents for adsorption capacity, equilibrium adsorption time, and pH value.

Adsorbents type	Adsorption capacity(mg/g)	Adsorption equilibrium time(min)	pH range	References
$Ag_2Cu_2O_3$	735	90	3.5-11.5	This work
$Ag_2Cu_2O_4$	642	90	3.5-11.5	This work
Ag_2O-T3NT	571.1	10	4-7	1
Ag_2O-T3NL	431.5	60	7	2
Ag_2O-T3NF	381	60	7	1
$Ag_2O@Mg (OH)_2$	380.7	<10	6	3
$Ag°/Ag_2O$	326	1800	6-7	4
Ag_2O-$Na_2Nb_2O_6·H_2O$	291.9	100	6-9	5
3D Ag_2O-Ag/TiO_2	208	300	---	6
AgCl@CM	193.7	20	2_10	7
AgAero	88	420	7-9.5	8
MXene-PDA-Ag_2O_x	80	480	5	9
Bimetallic AgCu/Cu_2O hybrid	66	240	3	10
1.0%-Ag@Cu_2O	25.4	90	3-11	11
25%-Ag@MIL-101	2.14	180	3-10	12

Table S2. Langmuir and Freundlich isotherm parameters for the adsorption of I^-.

Adsorbent	Langmuir model			Freundlich model		
	q_m(mg/g)	K_L	R^2	K_F	$1/n$	R^2
Ag₂Cu₂O₃	734.3	0.4256	0.9999	5.1794	0.23976	0.5936
Ag₂Cu₂O₄	678	0.0232	0.994	3.1691	0.47454	0.79452

Table S3. Pseudo-first-order and Pseudo-second-order kinetics model constants of bimetallic Ag-Cu oxides for the adsorption of I^-.

Adsorbent	Concentration (mM)	Pseudo-first-order model			Pseudo-second-order model		
		R_1^2	q_e	K_1	R_1^2	q_e	K_2
Ag₂Cu₂O₃	5	0.0562	13.8465	0.0694	0.9999	602.4096	0.0205
Ag₂Cu₂O₄	5	0.2533	82.353	0.0781	0.9889	515.4639	0.0091

Table S4. Comparison of glucose detection performances using various CuO-based electrodes.

CuO nanostructures	Detection potential (V, vs. Ag/AgCl)	Linear range	Sensitivity(μA $cm^{-2}mM^{-1}$)	LOD(μM)	References
Porous CuO derived from Ag₂Cu₂O₃	0.55	0.01 μM-4.96 mM	4615.26	0.4	This work
Porous CuO derived from Ag₂Cu₂O₄	0.55	0.01 μM-5.96 mM	4241.63	0.48	This work
CuO nanowires	0.33	0.4μM-2.0 mM	490	0.049	13
CuO nanospheres	0.6	up to 2.55 mM	404.53	1	14
CuO/MWCNTs	0.4	0.4 μM-	2596	0.2	15

		1.2 mM			
CuO nanoplatelets	0.55	up to 0.80 mM	3490.7	0.5	16
CuO–SWCNT	0.495	0.05 µM-1.8 mM	1610	0.05	17
CuO nanoellipsoids	0.55	100 µM-3.0 mM	2555	0.072	18
CuO nanowires	0.55	---	684.2	2	19
Hollow CuO polyhedrons	0.55	up to 4.0 mM	1112	0.33	20
3D porous CuO nanowires	0.35	up to 2.55 mM	1420.3	5.1	21
CuO nanoparticles/ITO	0.59	up to 4.4 mM	450.2	0.7	22
CuO nanorods	0.55	100 µM-4.0 mM	1834	0.22	23
Porous CuO nanobelts	0.5	0.1 µM-2.0 mM	1876.52	0.06	24
CuBr@CuO nanoparticles	0.345	5.0 µM-3.51 mM	3096	1.44	25
CuO nanorod@PCFs	0.6	5.0 µM-0.8 mM	608.9	5	26
CuO nanoparticles-CSs/GCE	0.55	0.5 µM-2.3 mM	2981	0.5	27
CuO@C/D	0.5	0.5 µM-4 mM	1650	0.5	28

Table S5. Amperometric response of the porous CuO nanostructure electrodes toward 0.1 mM interferents at 0.55 V (vs. SCE) in the absence and presence of 1.0 mM glucose in 0.1 M NaOH.

	CuO electrodes from $Ag_2Cu_2O_3$		CuO electrodes from $Ag_2Cu_2O_4$	
Interferents	Response(mA)	ratio	Response(mA)	ratio
Glucose	0.434493		0.379117	
Lactose	0.47	8.17%	0.416808	9.94%
Galactose	0.505	7.45%	0.448727	7.66%
Sucrose	0.544	7.75%	0.48438	7.94%
Fructose	0.572	5.12%	0.508829	5.05%
NaCl	0.58	1.38%	0.512564	0.73%
Uric acid	0.576	0.69%	0.510526	0.41%

Table S6. Main composition of the synthetic seawater used in this work (pH 8.15).

Composition	Concentration (g/L)
Na^+	10.833
K^+	0.369
Ca^{2+}	0.544
Mg^{2+}	2.736
SO_4^{2-}	2.707
HCO_3^-	0.145
Cl^-	23.928

References

(1)   Yang, D.; Sarina, S.; Zhu, H.; Liu, H.; Zheng, Z.; Xie, M.; Smith, S. V.; Komarneni, S. Capture of Radioactive Cesium and Iodide Ions from Water by Using Titanate Nanofibers and Nanotubes. *Angew. Chemie - Int. Ed.* **2011**, *50* (45), 10594–10598.

(2)   Bo, A.; Sarina, S.; Zheng, Z.; Yang, D.; Liu, H.; Zhu, H. Removal of Radioactive Iodine from Water Using Ag2O Grafted Titanate Nanolamina as Efficient Adsorbent. *J. Hazard. Mater.* **2013**, *246–247*, 199–205.

(3)   Chen, Y. Y.; Yu, S. H.; Yao, Q. Z.; Fu, S. Q.; Zhou, G. T. One-Step Synthesis of $Ag_2O@Mg(OH)_2$ Nanocomposite as an Efficient Scavenger for Iodine and Uranium. *J.*

Colloid Interface Sci. **2018**, *510*, 280–291.

(4)   Baimenov, A. Z.; Berillo, D. A.; Inglezakis, V. J. Cryogel-Based Ag°/Ag$_2$O Nanocomposites for Iodide Removal from Water. *J. Mol. Liq.* **2020**, *299*, 112134.

(5)   Mu, W.; Li, X.; Liu, G.; Yu, Q.; Xie, X.; Wei, H.; Jian, Y. Safe Disposal of Radioactive Iodide Ions from Solutions by Ag$_2$O Grafted Sodium Niobate Nanofibers. *Dalt. Trans.* **2016**, *45* (2), 753–759.

(6)   Liu, S.; Wang, N.; Zhang, Y.; Li, Y.; Han, Z.; Na, P. Efficient Removal of Radioactive Iodide Ions from Water by Three-Dimensional Ag$_2$O-Ag/TiO$_2$ Composites under Visible Light Irradiation. *J. Hazard. Mater.* **2014**, *284*, 171–181.

(7)   Li, Q.; Mao, Q.; Li, M.; Zhang, S.; He, G.; Zhang, W. Cross-Linked Chitosan Microspheres Entrapping Silver Chloride via the Improved Emulsion Technology for Iodide Ion Adsorption. *Carbohydr. Polym.* **2020**, *234*, 115926.

(8)   Asmussen, R. M.; Matyáš, J.; Qafoku, N. P.; Kruger, A. A. Silver-Functionalized Silica Aerogels and Their Application in the Removal of Iodine from Aqueous Environments. *J. Hazard. Mater.* **2019**, *379*, 119364.

(9)   Huang, H.; Sha, X.; Cui, Y.; Sun, S.; Huang, H.; He, Z.; Liu, M.; Zhou, N.; Zhang, X.; Wei, Y. Highly Efficient Removal of Iodine Ions Using MXene-PDA-Ag$_2$O$_x$ Composites Synthesized by Mussel-Inspired Chemistry. *J. Colloid Interface Sci.* **2020**, *567*, 190–201.

(10)   Mao, P.; Liu, Y.; Liu, X.; Wang, Y.; Liang, J.; Zhou, Q.; Dai, Y.; Jiao, Y.; Chen, S.; Yang, Y. Bimetallic AgCu/Cu$_2$O Hybrid for the Synergetic Adsorption of Iodide from Solution. *Chemosphere* **2017**, *180*, 317–325.

(11)   Mao, P.; Liu, Y.; Jiao, Y.; Chen, S.; Yang, Y. Enhanced Uptake of Iodide on Ag@Cu$_2$O Nanoparticles. *Chemosphere* **2016**, *164*, 396–403.

(12)   Mao, P.; Qi, B.; Liu, Y.; Zhao, L.; Jiao, Y.; Zhang, Y.; Jiang, Z.; Li, Q.; Wang, J.; Chen, S.; Yang, Y. AgII Doped MIL-101 and Its Adsorption of Iodine with High Speed in Solution. *J. Solid State Chem.* **2016**, *237*, 274–283.

(13)   Zhuang, Z.; Su, X.; Yuan, H.; Sun, Q.; Xiao, D.; Choi, M. M. F. An Improved Sensitivity Non-Enzymatic Glucose Sensor Based on a CuO Nanowire Modified Cu Electrode. *Analyst* **2008**, *133* (1), 126–132.

(14)   Reitz, E.; Jia, W.; Gentile, M.; Wang, Y.; Lei, Y. CuO Nanospheres Based Nonenzymatic Glucose Sensor. *Electroanalysis* **2008**, *20* (22), 2482–2486.

(15)   Jiang, L. C.; Zhang, W. De. A Highly Sensitive Nonenzymatic Glucose Sensor Based on CuO Nanoparticles-Modified Carbon Nanotube Electrode. *Biosens. Bioelectron.* **2010**,

25 (6), 1402–1407.

(16) Wang, J.; Zhang, W. De. Fabrication of CuO Nanoplatelets for Highly Sensitive Enzyme-Free Determination of Glucose. *Electrochim. Acta* **2011**, *56* (22), 7510–7516.

(17) Quoc Dung, N.; Patil, D.; Jung, H.; Kim, D. A High-Performance Nonenzymatic Glucose Sensor Made of CuO-SWCNT Nanocomposites. *Biosens. Bioelectron.* **2013**, *42* (1), 280–286.

(18) Zhang, X.; Sun, S.; Lv, J.; Tang, L.; Kong, C.; Song, X.; Yang, Z. Nanoparticle-Aggregated CuO Nanoellipsoids for High-Performance Non-Enzymatic Glucose Detection. *J. Mater. Chem. A* **2014**, *2* (26), 10073–10080.

(19) Zhang, Y.; Liu, Y.; Su, L.; Zhang, Z.; Huo, D.; Hou, C.; Lei, Y. CuO Nanowires Based Sensitive and Selective Non-Enzymatic Glucose Detection. *Sensors Actuators, B Chem.* **2014**, *191*, 86–93.

(20) Kong, C.; Tang, L.; Zhang, X.; Sun, S.; Yang, S.; Song, X.; Yang, Z. Templating Synthesis of Hollow CuO Polyhedron and Its Application for Nonenzymatic Glucose Detection. *J. Mater. Chem. A* **2014**, *2* (20), 7306–7312.

(21) Huang, J.; Zhu, Y.; Yang, X.; Chen, W.; Zhou, Y.; Li, C. Flexible 3D Porous CuO Nanowire Arrays for Enzymeless Glucose Sensing: In Situ Engineered versus Ex Situ Piled. *Nanoscale* **2015**, *7* (2), 559–569.

(22) Wang, T.; Su, W.; Fu, Y.; Hu, J. Controllably Annealed CuO-Nanoparticle Modified ITO Electrodes: Characterisation and Electrochemical Studies. *Appl. Surf. Sci.* **2016**, *390*, 795–803.

(23) Gou, X.; Sun, S.; Yang, Q.; Li, P.; Liang, S.; Zhang, X.; Yang, Z. A Very Facile Strategy for the Synthesis of Ultrathin CuO Nanorods towards Non-Enzymatic Glucose Sensing. *New J. Chem.* **2018**, *42* (8), 6364–6369.

(24) Li, Y. Y.; Kang, P.; Wang, S. Q.; Liu, Z. G.; Li, Y. X.; Guo, Z. Ag Nanoparticles Anchored onto Porous CuO Nanobelts for the Ultrasensitive Electrochemical Detection of Dopamine in Human Serum. *Sensors Actuators, B Chem.* **2021**, *327*, 128878.

(25) Lin, W. J.; Lin, Y. S.; Chang, H. T.; Unnikrishnan, B.; Huang, C. C. Electrocatalytic CuBr@CuO Nanoparticles Based Salivary Glucose Probes. *Biosens. Bioelectron.* **2021**, *194*, 113610.

(26) Li, M.; Zhao, Z.; Liu, X.; Xiong, Y.; Han, C.; Zhang, Y.; Bo, X.; Guo, L. Novel Bamboo Leaf Shaped CuO Nanorod@hollow Carbon Fibers Derived from Plant Biomass for Efficient and Nonenzymatic Glucose Detection. *Analyst* **2015**, *140* (18), 6412–6420.

(27) Zhang, J.; Ma, J.; Zhang, S.; Wang, W.; Chen, Z. A Highly Sensitive Nonenzymatic

Glucose Sensor Based on CuO Nanoparticles Decorated Carbon Spheres. *Sensors Actuators, B Chem.* **2015**, *211*, 385–391.

(28)   Zhai, Z.; Leng, B.; Yang, N.; Yang, B.; Liu, L.; Huang, N.; Jiang, X. Rational Construction of 3D-Networked Carbon Nanowalls/Diamond Supporting CuO Architecture for High-Performance Electrochemical Biosensors. *Small* **2019**, *15* (48),1901527.